



# Dynamic and large field of view photonic resonator absorption microscopy for ultrasensitive digital resolution detection of nucleic acid and protein biomarkers

Weinan Liu<sup>a,b</sup>, Takhmina Ayupova<sup>b,c</sup>, Weijing Wang<sup>b,c</sup>, Skye Shepherd<sup>b,c</sup>, Xiaojing Wang<sup>b,c</sup>, Lucas D. Akin<sup>d</sup>, Manish Kohli<sup>e</sup>, Utkan Demirci<sup>f</sup>, Brian T. Cunningham<sup>a,b,c,d,g,h,\*</sup>

<sup>a</sup> Department of Electrical and Computer Engineering, University of Illinois at Urbana-Champaign, Urbana, IL, 61801, USA

<sup>b</sup> Nick Holonyak Jr. Micro and Nanotechnology Laboratory, Urbana, IL, 61801, USA

<sup>c</sup> Department of Bioengineering, University of Illinois at Urbana-Champaign, Urbana, IL, 61801, USA

<sup>d</sup> Department of Chemistry, University of Illinois at Urbana-Champaign, Urbana, IL, 61801, USA

<sup>e</sup> Huntsman Cancer Institute, University of Utah, Salt Lake City, UT, 84112, USA

<sup>f</sup> Department of Radiology, Department of Electrical Engineering (by Courtesy), Stanford University, Palo Alto, CA, 94304, USA

<sup>g</sup> Carl R. Woese Institute for Genomic Biology, Urbana, IL, 61801, USA

<sup>h</sup> Cancer Center at Illinois, Urbana, IL, 61801, USA

## ARTICLE INFO

### Keywords:

Digital-resolution biosensing  
Cancer biomarker  
Antibody detection  
Dynamic assay  
Micro RNA

## ABSTRACT

In this paper, we describe a biosensing instrument based on our previously developed photonic resonator absorption microscope (PRAM) that incorporates autofocus, digital representation of the gold nanoparticle (AuNP) accumulation, and the ability to gather time-series image sequences of AuNP attachment and detachment from the photonic crystal (PC) surface. The combined capabilities are used to fully automate PRAM image collection during biomolecular assays to enable tiling of PRAM images to provide millimeter-scale field of view. The instrument can also gather PRAM “movies” that enables digital showcasing and dynamic counting AuNPs as they arrive and depart from the PC surface. We utilize the capabilities in the context of two biomolecular assays for detection of protein biomarkers in a conventional AuNP-tagged sandwich format. Utilizing dynamic counting of AuNP attachment and detachment events during the assay we present a detection for microRNA-375 (miRNA-375) down to 1 aM with a 10-min, room temperature, enzyme-free approach, while revealing characteristics of the binding-rate and unbinding-rate of the biomolecular interactions. Our instrument can potentially find broad applications in multiplexed point-of-care diagnostic testing, and as a general-purpose tool for quantitative characterization of biomolecular binding kinetics with single-molecule resolution.

## 1. Introduction

In previous papers, we described Photonic Resonator Absorption Microscopy (PRAM) in which gold nanoparticle (AuNP) tags with a localized surface plasmon resonance (LSPR) wavelength that overlaps with the guided mode resonant reflection wavelength of a photonic crystal (PC) surface (Huang et al., 2020a, 2020b; Huang and Cunningham, 2019; Liu et al., 2017). Through enhanced optical absorption, each AuNP that is attached to the PC surface results in highly localized reduction in the reflected intensity that can be easily measured by illuminating the PC from below with a low intensity LED with a wavelength that also overlaps with the PC resonant wavelength. While the

initial implementation of PRAM utilized line scanning and spectral imaging to analyze the reflected resonant spectrum in an approach that required ~2 min to collect and analyze each image (Canady et al., 2019; Zhuo and Cunningham, 2015; Zhuo et al. 2014a, 2014b), we demonstrated the ability to make the PRAM instrument less expensive and more portable by eliminating the spectrometer, to simply gather whole-frame images of the reflected resonant intensity (Ghosh et al., 2021). In our previously reported “portable PRAM” (p-PRAM) instrument, the PC biosensor was mounted upon a 3-axis (x, y, z) manually adjusted translation stage that required the operator to adjust the PC surface into the focus plane. As we consider the application of PRAM for point-of-care diagnostics and life science research applications where

\* Corresponding author. Department of Electrical and Computer Engineering, University of Illinois at Urbana Champaign, Urbana, IL, 61801, USA.  
E-mail address: [bcunning@illinois.edu](mailto:bcunning@illinois.edu) (B.T. Cunningham).

<https://doi.org/10.1016/j.bios.2024.116643>

Received 3 April 2024; Received in revised form 31 July 2024; Accepted 6 August 2024

Available online 8 August 2024

0956-5663/© 2024 Elsevier B.V. All rights reserved, including those for text and data mining, AI training, and similar technologies.

the instrument would be utilized by clinicians, biologists, and biochemists, it is important for the system to be automated to remove tedious repetitive tasks from the user, while also providing capabilities that will make PRAM assays more quantitatively accurate and repeatable. Further, the ability to image and count the arrival and departure of AuNP-tagged binding events opens the potential utilization of PRAM for more clearly understanding the factors that limit the rates of biomarker accumulation on the sensor.

In this work, we describe an automated portable PRAM (ap-PRAM) instrument that integrates computer-controlled motorized translation stages and time-series image collection, enabling rapid automatic biomarker detection, extended field of view (FOV) tiling, and single molecule kinetic analysis. By gathering time-series PRAM images from a single FOV, we demonstrate the capability of the ap-PRAM to digitally count the arrival and departure of each AuNP between temporally adjacent image frames. We demonstrate the dynamic counting

capability of ap-PRAM in the context of two assay formats. First, we perform detection of viral antibodies (anti-HIV and anti-HCV) in a sandwich format, in which the target antibody is captured to the PC surface by an immobilized selective antigen, while AuNPs prepared with an immobilized secondary label antibody bind with the target antibody at a separate epitope. Second, we perform detection of a representative cancer-associated miRNA biomarker (miRNA-375) using a Target Recycling Amplification Process (TRAP) described fully in a prior report (Wang et al., 2023). Using the ap-PRAM dynamic detection capability, the rates of arrival and release of AuNPs during the TRAP process can be observed with single AuNP precision, with kinetic characteristics, dictated by thermodynamics and diffusion, that have distinct characteristics compared to the protein-protein interactions that occur in the sandwich assay. Although not discussed in this report, the ap-PRAM facilitates multiplexed detection of assays that are performed in an array of PC biosensor liquid compartments, such as microfluidic

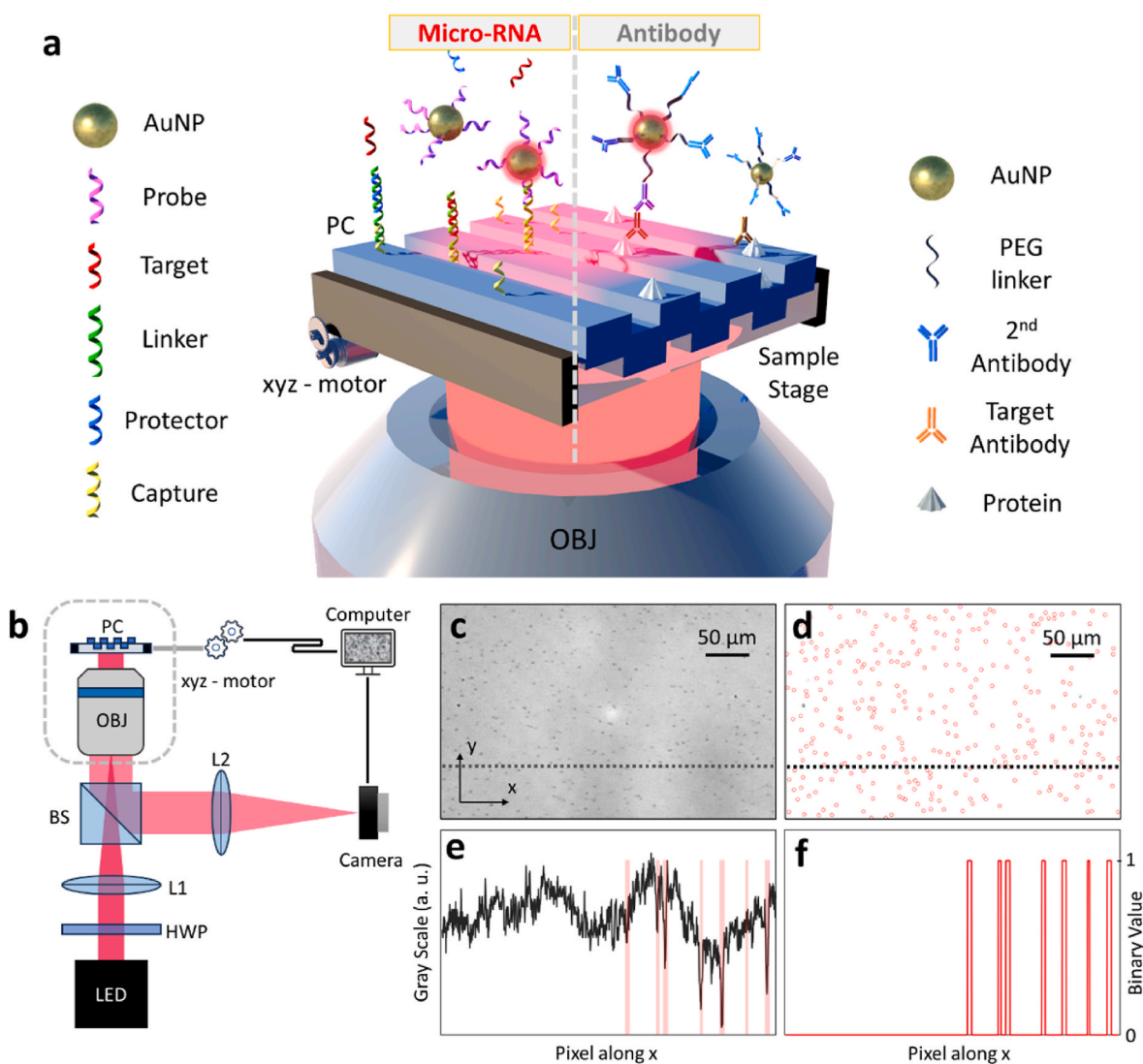


**Fig. 1.** Automated portable photonic resonator absorption microscope (ap-PRAM). **a.** Schematic illustration of ap-PRAM detection for microRNA (miRNA) and antibody using target recycling amplification process (TRAP) assay and sandwich assay, respectively. **b.** Optical and mechanical setup of ap-PRAM. A red LED emitting collimated light is focused on the back focal plane of the objective. A half wave plate is used to rotate the polarization to align with the PC TM polarization incidence requirement. Reflected light containing regions of reduced intensity due to AuNP attachment are gathered on the image sensor, which communicates with the computer controlling the motorized sample stage. OBJ: objective. BS: beam splitter. L: lens. HWP: half wave plate. **c.** An example raw ap-PRAM image. The image shows the point spread function of the AuNPs since the size of the AuNP is just  $\sim 1/4$  of the diffraction-limited resolution. **d.** Processed ap-PRAM image where the background is completely deleted, and each circle indicates an AuNP in the same location as the recognized AuNP in **c.** **e.** 1D ap-PRAM image gray scale versus pixel along x direction, evaluated from the dotted line in **c.** **f.** 1D ap-PRAM processed image versus pixel along x direction, evaluated from the dotted line in **d.**

cartridges (Che et al., 2019) or microplate wells, where the PC can be easily translated to a series of locations with automated sequences and autofocus to remove hands-on tasks from the operator. The ap-PRAM instrument represents an advance in the capabilities of biosensor microscopy, particularly for digital-resolution observation and quantitation of biomolecular assays for applications in diagnostics and life science research.

## 2. Results and discussion

### 2.1. Automated portable PRAM

The ap-PRAM consists of three parts: p-PRAM, programmed motorized translational stage, and the PC biosensor, as illustrated in Fig. 1a and b. The programmable motion stage is combined with a Thorlabs 12 mm Motorized Translation Stage (MT1-Z8) for the z-axis, two Thorlabs 25 mm Motorized Translation Stage (PT1-Z8) for the xy-axes, and a custom 3D-printed sample-holding stage designed to enable the PC to be positioned at a precise initial location. The  $2 \times 3 \text{ mm}^2$  PC biosensor is attached to a  $24 \times 60 \text{ mm}^2$  glass substrate with UV-curable adhesive.

The PC resonant reflected wavelength of 623 nm when the surface is covered with water is well matched to the 623 nm LSPR wavelength of the AuNP (80 nm gold nanourchins, Cytodiagnostics), as shown in Supplementary Fig. S1. The z-translation stage is utilized to automate the process of locating the focal plane, while the xy stages scan the sensing area to capture ap-PRAM images as shown in Fig. 1c and the intensity at certain row of the image sensor is shown in Fig. 1e. After image capture, an updated image processing algorithm, described in Supplementary Figs. S2–S4, identifies locations with reduced intensity compared to the surrounding area to enumerate the number of AuNPs in the image, as shown in Fig. 1d and the processed image at corresponding row of the image is shown in Fig. 1f.

### 2.2. Autofocus and field of view tiling

Autofocus is a required function for automated detection, and autofocus is especially important when the objective horizontally translates across the sample surface or during long term continuous observation of a kinetic assay (Pinkard et al., 2019). To develop automated scanning and long-term focused recording functions for

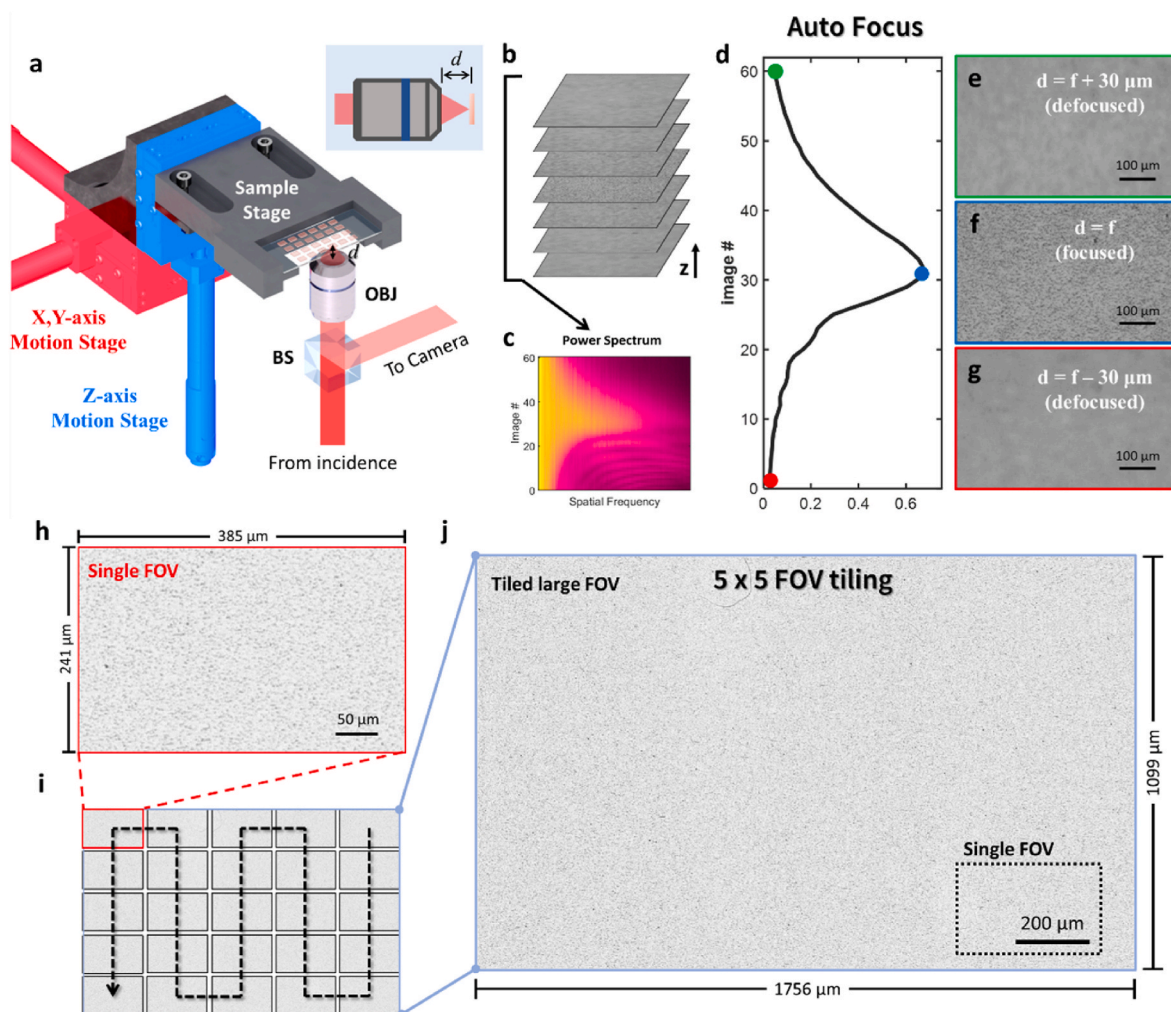


**Fig. 2.** Schematic illustration of the autofocus module and its working principle. **a.** Motion stages (z-axis highlighted), 3D printed sample holding stage and part of the ap-PRAM optical setup, where  $d$  is the distance from the PC to the OBJ, as shown in the inset. **b.** Focal stack generated from scanning 61 images around the focal plane with  $1 \mu\text{m}$  intervals. **c.** Radially averaged power spectrum (RAPS) calculated from the focal stack. **d.** Integrations of the high-frequency component of RAPS for the focal stack, where a single peak curve was demonstrated. The green, blue, and red dots indicate the imaging planes at  $+30 \mu\text{m}$ ,  $0 \mu\text{m}$ , and  $-30 \mu\text{m}$  away from the focal plane and shown as blurry, sharp, and blurry again. **e-g.** Ap-PRAM images captured at positions corresponding to the green (e), blue (f), and red (g) dot in d. **h.** Single FOV ( $385 \times 241 \mu\text{m}^2$ ) of AuNPs captured by ap-PRAM autofocus imaging. **i.**  $5 \times 5$  FOV stitching following a zigzag path. **j.** With a 10 percent overlap between two neighboring FOVs,  $5 \times 5$  FOV tiling can generate a  $21 \times$  larger final image with size of  $1756 \times 1099 \mu\text{m}^2$ . The resolution was preserved even though image size increased (see Supplementary Fig. S8). **Figures h-j** have been processed by background filtering.

ap-PRAM, we programmed the z-axis motion stage to communicate with the focus measure calculated from the currently captured image, and translate the direction leading to a higher focus measure. Fig. 2a schematically demonstrates the autofocus module, where  $d$  is the distance between the objective and the upper surface of the PC. By driving the z-axis motor translation in 1  $\mu\text{m}$  steps, 61 images were acquired near the focal plane, as shown in Fig. 2b. Next, we calculated the focus measure by integration of the high-frequency component of the focal stack's radially averaged power spectrum (RAPS) (Fig. 2c), resulting in the single peak curve presented in Fig. 2d. The focal plane, which lies near the 30th image, is marked as a blue circle, and two other defocused planes are marked as green and red circles, respectively, as correspondingly shown as Fig. 2e–g. By computing and comparing the focus measure of the image below and above the current imaging plane the software that drives the z-translation stage will command the stage to move to the correct position. In Supplementary Information, the details of the autofocus program are shown based on this principle (Figs. S5 and S6).

The size of a single FOV is  $385 \times 241 \mu\text{m}^2$ , while the sensing area of a PC as the bottom of a  $\sim 20 \mu\text{l}$  well is nearly 70 times larger (Ghosh et al., 2021), and thus a single FOV measures only a fraction of the entire sensor surface. Nonuniform binding of AuNPs may induce inconsistent reporting of AuNP density, since the binding situation may differ from one FOV to another due to unpredictable experimental variables induced by pipetting, surface functionalization nonuniformity, nearness to the edge of the well, blocking efficiency, or mixing. Thus, detection from a large FOV enables more quantitatively accurate and representative determination of binding events (Mahecic et al., 2020). While a lower magnification objective will increase the size of the FOV, the spatial extent of the AuNPs in the PRAM image will be reduced accordingly. Taking advantage of the horizontal translation stage and efficient autofocus modules, we developed a FOV tiling method to substantially increase the FOV while utilizing 50x objective lens (OLYMPUS) (Supplementary Fig. S7). By setting a small portion (10%) of the FOV as an overlapping region on the perimeter of neighboring FOVs, our image processing approach can automatically align and tile multiple FOVs into one larger PRAM image, meanwhile trimming the overlapping regions to present a final image without seams or gaps at the FOV borders. An example of  $5 \times 5$  ap-PRAM tiling image is shown in Fig. 2h–j, where 25 FOVs were autofocused and captured in a zig-zag path and finally merged into a tiled image with a size of  $1.756 \times 1.099 \text{ mm}^2$ , which is 20.8 folds larger than a single FOV. By quantitatively comparing the results of single capture and tiled  $3 \times 3$  PRAM images we demonstrated how the FOV stitching method reduced the error from uneven AuNP binding distribution, and discussed its processing efficiency in the Supplementary Information (Fig. S8 and Table S1).

### 2.3. Dynamic monitoring of sandwich assay for an antibody target and a target recycling strand displacement assay for miRNA detection

To clearly visualize the dynamics of binding and unbinding events in which AuNPs are used as a tag, we developed a differential detection algorithm, described in supplementary information (Fig. S9), that enables each event to be counted with single-AuNP resolution. We incubate the HIV/HCV antigen (overnight at  $4^\circ\text{C}$ ) with the test sample and secondary antibody-functionalized gold nanoparticles ( $2^\circ\text{Ab-AuNPs}$ ) in a one-pot, single step detection approach that does not utilize enzymatic amplification or a washing step to remove nonspecific binding. The reagents are introduced to the well with the PC biosensor as the bottom surface, followed by initiation of ap-PRAM image collection. No stirring or shaking is applied. The recombinant viral protein-coated PC biosensor serves as a surface for formation of sandwich immunocomplex through specific antigen–antibody interactions (Fig. 3a). We recorded and processed 1h ap-PRAM video gathered at 30 s intervals for a high concentration of 10  $\mu\text{g/ml}$  HIV and HCV antibodies in buffer, as shown

in Fig. 3b (processed videos shown in Supplementary Information, Video S2 and S3). The concentration of Ab-functionalized AuNPs in the assay is Abs (625 nm) =  $1.2 \pm 0.1$  at a volume of 18  $\mu\text{L}$ , and the total assay volume is 20  $\mu\text{L}$ . The binding and unbinding data are plotted in Fig. 3c and d for HIV and HCV antibodies, respectively. We observe that both anti-HIV and anti-HCV detection reactions are dominated by binding events, and unbinding is negligible. We observe that after 60 min, equilibrium is not reached as the density of AuNPs on the PC surface continues to accumulate as neither the target antibody nor AuNPs are exhausted. This assay reveals that very few immunocomplexes disassemble due to the high binding affinity of antibody interactions with their corresponding antigen. We also demonstrated the low concentration (10 ng/mL or 66.6 pM) detection of anti-HCV, as shown in Fig. 3e. We compared the assay detection to the blank sample and observed that in the near-limit concentration, the accumulated AuNP difference between the assay and blank sample were decreased compared to that of the high concentration sample. Meanwhile, we also observed more unbinding events compared to the high concentration sample. Note that over the course of 1 h of assay incubation time,  $\sim 150$  AuNPs accumulate on the PC biosensor surface as nonspecific binding for the “blank” measurement. This number of nonspecific AuNPs does not actually represent a high number, although the presence of a nonzero nonspecific binding rate must be used as a reference against which specific binding must be accounted for. To avoid overcounting induced by nonspecific binding (nonspecifically and specifically bound AuNPs were all recognized), we conducted a binding kinetics assay using streptavidin-conjugated AuNPs and a biotin-functionalized PC, as shown in Supplementary Fig. S10.

Supplementary video related to this article can be found at <https://doi.org/10.1016/j.bios.2024.116643>

miRNAs are noncoding RNAs that regulate gene expression at a post transcriptional level in several tumor types (Dai et al., 2012; Faltejskova et al., 2012; He et al., 2012; Huang et al., 2015; Hudson et al., 2013; Tsukamoto et al., 2010; Wang et al., 2016; Zhou et al., 2012). Next, we investigated the TRAP assay (Wang et al., 2023) where target miRNAs are recycled to efficiently amplify the PRAM AuNP count, shown in Fig. 3f. The reaction mechanism is based on a series of toehold-mediated strand displacement reactions. In the absence of target miRNA, the DNA probes (pink) immobilized upon AuNPs cannot hybridize with their complementary base sequence on the linker strand (green) while it is blocked by a protector sequence (blue). When the specific miRNA target (red) is present, it reacts with an initial toehold region on the linker to remove the protector strand through a toehold-mediated strand displacement reaction, resulting in the exposure of a second toehold region on the terminal of the linker sequence. This exposed toehold then reacts with the probe DNA on the AuNPs to initiate a second strand displacement reaction. The binding of the probe sequence additionally triggers the release of the target miRNA, so as each AuNP is bound to the PC, the miRNA target is recycled to initiate a new round of strand displacement reactions, rapidly amplifying the number of AuNPs attached to the PC biosensor.

Using ap-PRAM we dynamically detected miRNA-375 with concentration ranging from 0 aM to 1 fM for 1 h at 30 s time intervals. The biosensor's response is shown in Fig. 3g. Here we observed completely distinct kinetics from the sandwich assay in which all five responses follow a linear relation with time, showing that the reaction rate is constant all the way to at least 60 min. The dynamic monitoring of the TRAP assay illustrates how well the DNA-fueled molecular machines of TRAP worked to enhance the sensing efficiency. First, we observed that unbinding contributes a significant portion of the net response as nucleic acid strand displacement reactions (shown in Fig. 3j), unlike antibody-antigen interactions, proceed in an equilibrium in which reverse reactions are more favorable, particularly when the concentration of the product is high. Although the binding and unbinding curves can be fit accurately with a quadratic function, their difference maintains a linear function versus time and was not affected by the number of AuNPs

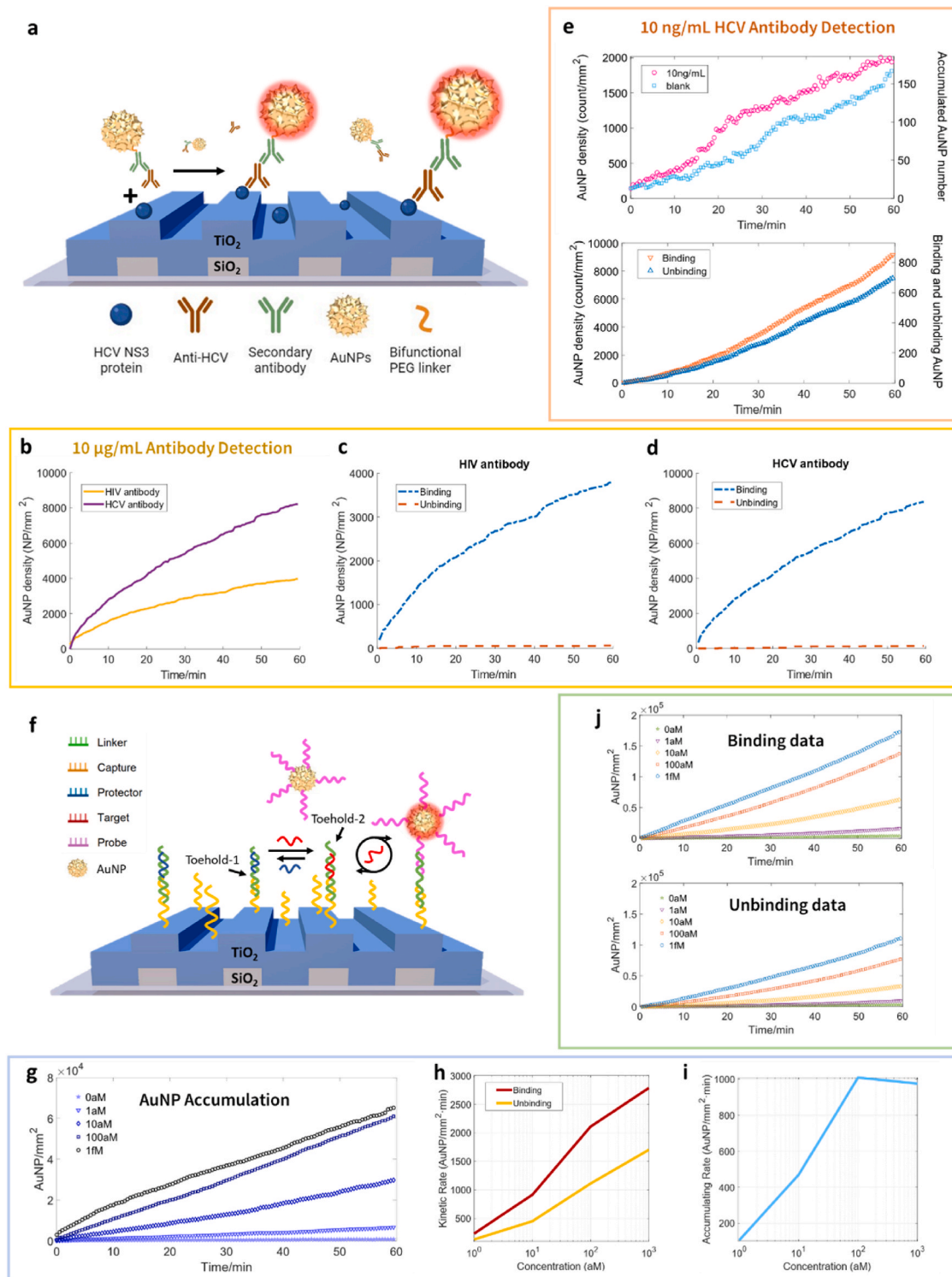


**Fig. 3.** ap-PRAM dynamic detection of a sandwich assay for detection of an antibody target and TRAP assay. **a.** Schematic illustration of the sandwich assay. **b.** Single-AuNP dynamics detection of 10 µg/mL HIV antibody assay and HCV antibody assay. **c.** and **d.** are the kinetic binding and unbinding of AuNP for HIV and HCV antibody assays, respectively. **e.** Dynamic detection of near-limit concentration (10 ng/mL) HCV antibody sandwich assay. Above: response of the assay (red dotted) compared to the blank sample (blue dotted). Below: Kinetic binding (orange triangle) and unbinding (blue triangle) AuNPs counted by differential counting algorithm. **f.** Schematic illustration of TRAP assay. DNA linker was hybridized with DNA capture and annealed with a protector. When target miRNA is introduced, protector is displaced and the linker-protectors is activated, resulting in the exposure of an additional DNA linker sequence (toehold-2). The probe sequence attached to the AuNP displaces the miRNA from the linker sequence and binds the AuNP to the PC surface, releasing the miRNA for target recycling. **g.** Overall sensor responses for miRNA-375 TRAP assay. Nonzero NP bound at the start of 1 fM was caused by a short recording delay. **h.** Calculated slope (rate) of AuNP binding and unbinding for 1 aM to 1 fM. **i.** Calculated slope (rate) of AuNP accumulation for 1 aM to 1 fM. **j.** Counted binding and unbinding events for miRNA-375 (concentration from 0 aM to 1 fM) TRAP assay.

captured, where in a single-toehold non-amplifying miRNA detection assay the accumulation rate would change over time (Canady et al., 2019). In the case that the concentration of target miRNA is as high as 1 fM, the reverse reaction becomes increasingly thermodynamically favorable, and we find from Fig. 3h that the accumulation rate reaches a plateau which is induced by the greater increment of the unbinding rate than the binding rate, as shown in Fig. 3i. Note that in an equilibrium binding interaction, such as the nucleic acid strand displacement reaction, the rate of the reverse process is increased in proportion to the concentration of the product, which in our case is the miRNA concentration. Meanwhile, the target miRNA is always recycled and maintained at a high concentration its initial concentration as the reaction proceeds, hence the reaction rate becomes much faster compared to a regular non-recycled reaction in which the target molecules are consumed when they are irreversibly captured during the detection process. The thermodynamics of the TRAP reaction is discussed in the Supplementary Information (shown in Supplementary Fig. S11). By plotting the net AuNP density at variable miRNA target concentrations, we observe the AuNP accumulation rate (calculated as the slope of the AuNP density versus time curve) enables us to observe small concentration differences between 1 aM and 2 aM that are not easily observable with the ordinary non-differential AuNP counting method (see Supplementary Fig. S12 and Table S2). The reproducibility of our sensor performance is shown in Supplementary Fig. S13.

### 3. Conclusion

We presented an automated portable PRAM (ap-PRAM) instrument which advanced the capabilities of original p-PRAM into an automatic system that is capable of rapid biomarker detection, extended field of view tiling, and digital resolution dynamic analysis of binding interactions that utilize an AuNP tag. We also improved the original image processing algorithm and developed a powerful differential detection algorithm that greatly suppressed noise, was able to differentiate close-spaced AuNPs to reveal the dynamic details of biosensing assays and simplified the representations of AuNPs' binding with binary figure. The differential algorithm is capable of counting AuNPs that bind to the PC surface and remain in place, as well as AuNPs that detach from the surface. A PC blocking protocol was performed to prevent nonspecific binding to retrieve true attachment of AuNPs. To demonstrate the differences between high and low dissociation constant  $K_d$ , we strategically selected antibody-antigen binding interaction ( $K_d \sim 1$  nM) and a DNA strand displacement reaction ( $K_d \sim 10^{-1}$   $\mu$ M) where unbinding is easily observable. Detection of viral antibodies (for HIV and HCV) in an AuNP-tagged sandwich assay format showed that the binding events are dominant and suggest that non-specific binding, which would be more likely to be observed by unbinding of surface-associated AuNPs, is a minimal factor, even with a high concentration of functionalized AuNPs in the assay volume. Furthermore, in this work the molecular dynamic detection of miRNA TRAP demonstrated the ability to differentiate 1 aM from 2 aM miRNA concentrations through observation of differences in AuNP accumulation rate. We expect the ap-PRAM instrument to facilitate adoption of PRAM for point-of-care diagnostics, personalized medicine, global health, and liquid biopsy approaches for cancer as well as applications in life science research.

### CRedit authorship contribution statement

**Weinan Liu:** Writing – review & editing, Writing – original draft, Visualization, Validation, Software, Methodology, Investigation, Formal analysis, Data curation, Conceptualization. **Takhmina Ayupova:** Writing – original draft, Visualization, Formal analysis, Data curation. **Weijing Wang:** Writing – original draft, Data curation. **Skye Shepherd:** Writing – original draft, Data curation. **Xiaoqing Wang:** Data curation.

**Lucas D. Akin:** Data curation. **Manish Kohli:** Resources. **Utkan Demirci:** Resources. **Brian T. Cunningham:** Writing – review & editing, Writing – original draft, Supervision, Project administration, Funding acquisition, Conceptualization.

### Declaration of competing interest

The authors declare that they have no known competing financial interests or personal relationships that could have appeared to influence the work reported in this paper.

### Data availability

Data will be made available on request.

### Acknowledgement

The authors gratefully acknowledge funding from the National Institutes of Health (R01EB029805, R33CA272271 and R21 HD111226). L.A. gratefully acknowledges support from a Cancer Center at Illinois (CCIL) philanthropic grant from the Bahl family.

### Appendix A. Supplementary data

Supplementary data to this article can be found online at <https://doi.org/10.1016/j.bios.2024.116643>.

### References

- Canady, T.D., Li, N., Smith, L.D., Lu, Y., Kohli, M., Smith, A.M., Cunningham, B.T., 2019. Proceedings of the National Academy of Sciences 116 (39), 19362.
- Che, C., Li, N., Long, K.D., Aguirre, M.A., Canady, T.D., Huang, Q., Demirci, U., Cunningham, B.T., 2019. Lab Chip 19 (23), 3943–3953.
- Dai, X., Chiang, Y., Wang, Z., Song, Y., Lu, C., Gao, P., Xu, H., 2012. Mol. Med. Rep. 5 (5), 1299–1304.
- Faltesjkova, P., Svoboda, M., Srutova, K., Milcochova, J., Besse, A., Nekvindova, J., Radova, L., Fabian, P., Slaba, K., Kiss, I., Vyzula, R., Slaby, O., 2012. J. Cell Mol. Med. 16 (11), 2655–2666.
- Ghosh, S., Li, N., Xiong, Y., Ju, Y.-G., Rathslag, M.P., Onal, E.G., Falkiewicz, E., Kohli, M., Cunningham, B.T., 2021. Biomed. Opt Express 12 (8), 4637–4650.
- He, X.X., Chang, Y., Meng, F.Y., Wang, M.Y., Xie, Q.H., Tang, F., Li, P.Y., Song, Y.H., Lin, J.S., 2012. Oncogene 31 (28), 3357–3369.
- Huang, Q., Canady, T., Gupta, R., Li, N., Singamaneni, S., Cunningham, B.T., 2020a. ACS Photonics 7 (8), 1994–2001.
- Huang, Q., Cunningham, B.T., 2019. Nano Lett. 19 (8), 5297–5303.
- Huang, Q., Li, N., Zhang, H., Che, C., Sun, F., Xiong, Y., Canady, T.D., Cunningham, B.T., 2020b. Lab Chip 20 (16), 2816–2840.
- Huang, X., Yuan, T., Liang, M., Du, M., Xia, S., Dittmar, R., Wang, D., See, W., Costello, B. A., Quevedo, F., Tan, W., Nandy, D., Bevan, G.H., Longenbach, S., Sun, Z., Lu, Y., Wang, T., Thibodeau, S.N., Boardman, L., Kohli, M., Wang, L., 2015. Eur. Urol. 67 (1), 33–41.
- Hudson, J., Duncavage, E., Tamburrino, A., Salerno, P., Xi, L., Raffeld, M., Moley, J., Chernock, R.D., 2013. Exp. Mol. Pathol. 95 (1), 62–67.
- Liu, J.N., Huang, Q., Liu, K.K., Singamaneni, S., Cunningham, B.T., 2017. Nano Lett. 17 (12), 7569–7577.
- Mahecic, D., Gambarotto, D., Douglass, K.M., Fortun, D., Banterle, N., Ibrahim, K.A., Le Guennec, M., Gónczy, P., Hamel, V., Guichard, P., Manley, S., 2020. Nat. Methods 17 (7), 726–733.
- Pinkard, H., Phillips, Z., Babakhani, A., Fletcher, D.A., Waller, L., 2019. Optica 6 (6), 794–797.
- Tsukamoto, Y., Nakada, C., Noguchi, T., Tanigawa, M., Nguyen, L.T., Uchida, T., Hijiya, N., Matsuura, K., Fujioka, T., Seto, M., Moriyama, M., 2010. Cancer Res. 70 (6), 2339–2349.
- Wang, X., Shepherd, S., Li, N., Che, C., Song, T., Xiong, Y., Palm, I.R., Zhao, B., Kohli, M., Demirci, U., Lu, Y., Cunningham, B.T., 2023. Angew. Chem. Int. Ed. 62 (16), e202217932.
- Wang, Y., Lieberman, R., Pan, J., Zhang, Q., Du, M., Zhang, P., Nevalainen, M., Kohli, M., Shenoy, N.K., Meng, H., You, M., Wang, L., 2016. Mol. Cancer 15 (1), 70.
- Zhou, J., Song, S., Cen, J., Zhu, D., Li, D., Zhang, Z., 2012. Oncol. Res. 20 (5–6), 197–203.
- Zhuo, Y., Cunningham, B.T., 2015. Sensors 15 (9), 21613–21635.
- Zhuo, Y., Hu, H., Chen, W., Lu, M., Tian, L., Yu, H., Long, K.D., Chow, E., King, W.P., Singamaneni, S., Cunningham, B.T., 2014a. The Analyst 139 (5), 1007–1015.
- Zhuo, Y., Tian, L., Chen, W., Yu, H., Singamaneni, S., Cunningham, B.T., 2014b. Annu Int Conf IEEE Eng Med Biol Soc 2014, 2069–2072.